Effective Viscosity in the Simulation of Spatially Evolving Shear Flows with Monotonic FCT Models

F. F. GRINSTEIN AND R. H. GUIRGUIS*

Laboratory for Computational Physics & Fluid Dynamics, Naval Research Laboratory, Washington, D.C. 20375

The global numerical diffusion of a model for the low-Mach-number simulation of free mixing layers is investigated. The numerical model solves the inviscid time-dependent conservation equations for mass, momentum, and energy for ideal gases. The equations are solved using an explicit Flux-Corrected Transport (FCT) algorithm, directional timestep-splitting techniques on structured grids, and appropriate inflow and outflow boundary conditions. Effective measurement of the numerical diffusion of the model in uniform grids is performed by comparison of the laminar spread of the simulated mixing layers with that predicted by boundary layer theory. The results show that the residual numerical diffusion of the FCT model can emulate physical viscosity for laminar shear flows at moderately high Reynolds numbers. The global numerical diffusion is not very sensitive to changes in free-stream velocity ratio and can be reduced in a predictable way by refining the grid spacing.   © 1992 Academic Press, Inc.

1. INTRODUCTION

Recent papers [1–6] have reported results of numerical simulations of subsonic, spatially evolving two- and three-dimensional planar shear layers using monotonic FCT models. The numerical model solves the time-dependent, compressible, inviscid conservation equations for mass, momentum, and energy in three dimensions in order to examine the evolution of large-scale coherent structures. The equations are solved numerically using a fourth-order phase-accurate FCT algorithm, directional timestep-splitting techniques on structured grids, and appropriate inflow and outflow boundary conditions [1, 2]. This approach has been shown to be adequate for simulating the moderate and high-Reynolds-number vorticity dynamics in the transition region of free flows and reproduces the large-scale features of the flow observed in the laboratory experiments, e.g., the asymmetric entrainment [3], the distribution of merging locations [4], the spreading rate of the mixing layers [5, 6], and the basic three-dimensional features of the vorticity dynamics [6, 7]. In this paper, we address some of the

numerical issues of resolution which are important for validations in the studies of physical mechanisms in these simulations.

A large-eddy-simulation approach is used to compute the evolution of the transitional flow dynamics. The nonlinear FCT high-frequency filtering, combined with the conservative, causal, and monotone properties of the algorithm, are expected to effectively provide a minimal subgrid model by maintaining the large-scale structures while numerically smoothing the scales with wavelengths smaller than a few computational cells. In this framework, the small residual numerical viscosity of the algorithm, combined with unresolved small-scale convection at high Reynolds numbers, mimics the behavior of physical viscosity.

The objective of this paper is to study the effective numerical diffusion of the algorithm in the low-Mach-number simulation of free mixing layers and its dependence on gridding and free-stream velocity ratio. A byproduct of this work is to assess the gridding requirements for an FCT-based shear-flow model including physical viscosity. In Section 2, we introduce the main steps of the FCT algorithm as used in the model and discuss the problem of measuring the residual numerical diffusion of the scheme. In Section 3.1, we review the calculation of the laminar spread of a free mixing layer based on boundary layer theory. The theoretical results are used as reference for the effective measurement of the global numerical diffusion of the model in Section 3.2. The final conclusions are given in Section 4.

2. THE FCT ALGORITHM

We restrict our discussion to the one-dimensional, explicit, fourth-order phase-accurate FCT algorithm [8] used in the shear-flow applications. The numerical model solves a system of generalized continuity equations of the form

$$\frac{\partial f}{\partial t} + \frac{\partial (vf)}{\partial r} = h, \tag{1}$$

---

* Current address: Detonation Physics Branch, Naval Surface Weapons Center, White Oak, MD 20903.

where f typically represents mass, momentum, or energy densities, h is an appropriate source term dependent on the flow variables and their spatial derivatives, v is the fluid velocity, and r is a spatial variable. The algorithm consists of a two-step predictor–corrector scheme which ensures that the conserved quantities remain monotonic and positive when so required. First, it modifies the linear properties of a high-order algorithm by adding diffusion during convective transport to prevent dispersive ripples from arising when sharp discontinuities are present. The added diffusion is then removed in the antidiffusion phase of the algorithm in such a way that the residual numerical diffusion is minimal while preserving the monotonicity and positivity of the scheme. The algorithmic details for the solution of Eq. (1) are discussed in general elsewhere [9]. In order to introduce the basic ideas it suffices here to restrict the discussion to the case of the mass density equation ($f = \rho$, $h = 0$), case for which the steps are briefly discussed below. In the first stage of the algorithm, the convection phase involves

$$f' = f_j^{(n)} - [\varepsilon_{j+1/2} f_{j+1/2}^{(n)} - \varepsilon_{j-1/2} f_{j-1/2}^{(n)}], \qquad (2a)$$

followed by the diffusion phase

$$\tilde{f}_j = f' + [v_{j+1/2}(f_{j+1}^{(n)} - f_j^{(n)}) - v_{j-1/2}(f_j^{(n)} - f_{j-1}^{(n)})], \qquad (2b)$$

where $f_j^{(n)}$ denotes the variable f at grid point j and timestep n, $j + 1/2$ denotes the midpoint between grid points j and $j + 1$,

$$\varepsilon_{j+1/2} = v_{j+1/2} \frac{\delta t}{\delta r}, \qquad (3)$$

δt and δr are the integration timestep and the grid spacing, respectively, and [8]

$$v_{j+1/2} = \tfrac{1}{6} + \tfrac{1}{3}\varepsilon_{j+1/2}^2. \qquad (4)$$

In turn, the correcting antidiffusion stage consists of

$$f_j^{(n+1)} = \tilde{f}_j - \hat{\Phi}_{j+1/2} + \hat{\Phi}_{j-1/2}, \qquad (5)$$

where the raw antidiffusion fluxes $\Phi_{j+1/2}$ are defined by

$$\Phi_{j+1/2} = \mu_{j+1/2}(f'_{j+1} - f'_j), \qquad (6)$$

and $\hat{\Phi}$ denotes the *corrected* antidiffusion flux. Monotonicity is preserved by the flux correction by ensuring that the diffusion compensation generates no new maxima or minima in the solution and existing extrema are not

accentuated [8]. In practice, this is enforced by defining the corrected fluxes as

$$\hat{\Phi}_{j+1/2}$$
$$= \mathrm{Max}[0, \mathrm{Min}(S(\tilde{f}_{j+2} - \tilde{f}_{j+1}), |\Phi_{j+1/2}|, S(\tilde{f}_j - \tilde{f}_{j-1}))], \qquad (7)$$

with $S = \mathrm{sign}(\tilde{f}_{j+1} - \tilde{f}_j)$, and $|S| = 1$.

In the schemes used in the FCT shear-flow models, the antidiffusion coefficients $\mu_{j+1/2}$ are defined in terms of a diffusion parameter, D_c, by

$$\mu_{j+1/2} = \tfrac{1}{6}D_c(1 - \varepsilon_{j+1/2}^2), \qquad (8)$$

where $D_c \lesssim 1$. For $D_c = 1$, the scheme reduces to the fourth-order *phoenical* FCT scheme [8]. A special case arises in the absence of convection, when $\varepsilon_{j+1/2} = 0$. In this case, in the vicinity of a sharp dicontinuity the antidiffusion flux $\Phi_{j+1/2}$ survives intact through the flux corrector and cancels the corresponding diffusion flux exactly if $D_c = 1$, in which case the discontinuity is preserved after the FCT cycle. Standard linear stability analysis shows that for $D_c < 1$ the scheme remains fourth-order-phase-accurate, and the amplitude accuracy becomes second-order, with the second-order error-term for the amplitude proportional to $(1 - D_c)$. Thus, by choosing D_c slightly smaller than unity (typically, $D_c = 0.997$–0.999 in the shear-flow applications) a small nonvanishing residual numerical diffusion can be provided by the scheme. A local estimate of the residual numerical diffusion introduced by D_c in the limit $v = 0$ has been communicated to the authors [10] and is briefly described in what follows. Combining (2) and (5) and comparing with the second-order, central-differenced version of the one-dimensional diffusion equation,

$$\frac{\partial f}{\partial t} - \mathscr{D} \frac{\partial^2 f}{\partial r^2} = 0, \qquad (9)$$

we can identify

$$\mathscr{D} \frac{\delta t}{(\delta r)^2} = \frac{1}{6}(1 - D_c), \qquad (10)$$

or equivalently, the diffusion coefficient is

$$\mathscr{D} = \frac{1}{6}(1 - D_c)\frac{(\delta r)^2}{\delta t}. \qquad (11)$$

Alternatively, we can rewrite this expression in a form useful in calculations performed with a fixed Courant number, $c = \delta t(|v| + a)_{\mathrm{peak}}/\delta r$,

$$\mathscr{D} = \frac{1}{6}(1 - D_c)\frac{\delta r(|v| + a)_{\mathrm{peak}}}{c}, \qquad (12)$$

where a is the local speed of sound. The inversely proportional dependence of $\mathscr{D}$ on c reflects the fact that a larger amount of residual numerical diffusion results from taking a lower value of c and correspondingly shorter timesteps.

Equations (11) and (12) give local estimates for the numerical diffusion of the algorithm in the absence of convection. Standard one-dimensional tests show that sharp discontinuities are maintained by the FCT algorithm and remain confined within 3–5 cells (e.g., Ref. [11]). This indicates that the actual residual numerical diffusion of the algorithm is nonlinear and somewhat dependent on the solution because of the flux correction. As a consequence, even if we enforce constant δr and c in the simulations—in which case Eq. (12) suggests that the concept of numerical diffusion can be physically meaningful—the effective (global) numerical diffusion in multidimensional spatially evolving shear-flow simulations cannot be estimated using straightforward extrapolations from one-dimensional local results. Thus, we need to obtain practical measures of the effects of numerical diffusion when nonlinear convection and compressibility are present, and when we have shear discontinuities rather than contact discontinuities. The present approach focuses on the initial laminar spread of a step-function velocity profile due to viscous (numerical) diffusion in the limit of low Mach numbers. In this case, we compare the results of the simulations with the known incompressible solution.

3. LAMINAR SPREADING OF THE MIXING LAYER

3.1. Boundary Layer Theory

We consider the laminar spread of a mixing layer initially defined by a step-function profile for the streamwise velocity
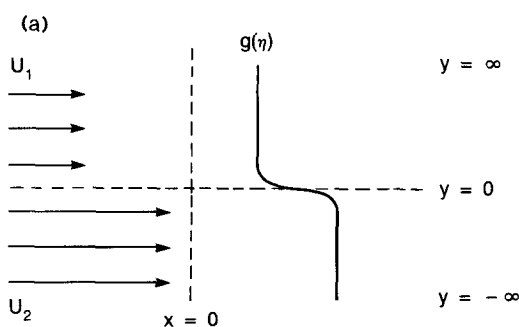
and zero transverse velocity. The flow configuration is indicated schematically in Fig. 1a, where the laminar spread of the velocity profile (as given by $g(\eta)$ for $x > 0$) can be calculated under certain flow conditions using boundary layer theory [12]. In this regime, the flow can be considered virtually incompressible, and the problem involves a thin shear layer with $v/u \ll 1$. Under these conditions, the pressure gradients are negligible and the steady-state incompressible equations describing the problem can be written

$$\frac{\partial u}{\partial x} + \frac{\partial v}{\partial y} = 0, \tag{13}$$

$$u\frac{\partial u}{\partial x} + v\frac{\partial u}{\partial y} - v\frac{\partial^2 u}{\partial y^2} = 0, \tag{14}$$

where v is the kinematical viscosity. The boundary conditions for the velocities in the steady state problem are specified by

$$u(0, y > 0) = U_1, \quad u(0, y < 0) = U_2, \quad v(0, y) = 0, \tag{15a}$$

$$u(x, y = +\infty) = U_1, \qquad v(x, y = +\infty) = 0, \tag{15b}$$

$$u(x, y = -\infty) = U_2, \qquad v(x, y = -\infty) = 0, \tag{15c}$$

with $U_2 > U_1$.

Defining the similarity variable

$$\eta = y(xv/U_2)^{-1/2}, \tag{16}$$

the solution can be expressed in terms of a function $G(\eta)$ related to the stream function Ψ and the velocities through

$$\Psi = (vxU_2)^{1/2} G(\eta), \tag{17}$$

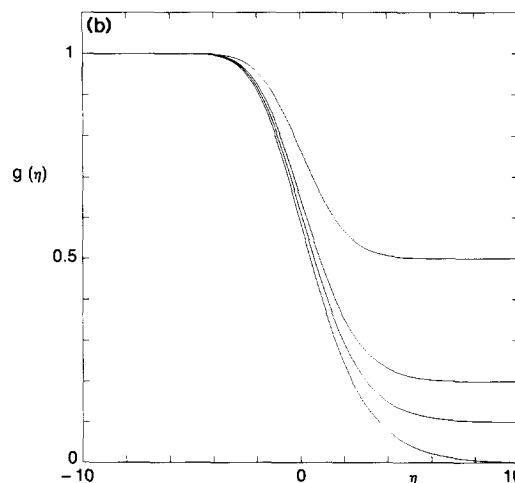$$u = U_2 \frac{dG(\eta)}{d\eta} = U_2 g(\eta). \tag{18}$$

FIG. 1. (a) Flow configuration for the theoretical study of the laminar spread of a mixing layer initialized at $x = 0$ with a step-function velocity profile; (b) mixing layer spread predicted by boundary layer theory for $\lambda = 2, 5, 10$, and ∞.

The function $G(\eta)$ satisfies the ordinary differential equation

$$G\frac{d^2G(\eta)}{d\eta^2}+2\frac{d^3G(\eta)}{d\eta^3}=0,\qquad(19)$$

which must be solved with the boundary conditions

$$G(0)=0;\quad G'(-\infty)=\lambda=U_2/U_1;\quad G'(+\infty)=1.\qquad(20)$$

Equation (14) is solved numerically using finite differences. Typical solutions obtained for the laminar spread of an incompressible mixing layer are shown in Fig. 1b for $\lambda=2$, 5, 10, ∞. These solutions are used as reference to measure the effective numerical (viscous) diffusion of the algorithm when simulating thin shear flows.

3.2. Simulated Mixing Layer

In order to talk about a meaningful effective numerical diffusion when $D_c \lesssim 1$ and measure its effects, we perform simulations for fixed Courant numbers in appropriate laminar flow cases using uniform grids in the regions of interest. We restrict our time-dependent simulations to the limit of low Mach numbers. In this limit, the flow is virtually incompressible and a comparison can be set with the results in Section 3.1 after attaining the steady-state regime using a time-marching approach. We seek a measure of the effective viscous diffusion by comparing the numerical spread of an initial step-function streamwise velocity profile with the laminar spread predicted by boundary layer theory. The choice of $D_c \lesssim 1$ is dictated by the interest in numerically simulating the large-scale features of transitional, free shear flows in the limit of large (but finite) Reynolds numbers, while maintaining the accuracy of the scheme as close to fourth order as possible. In the present study we have specially focused on the case $D_c = 0.999$, which has been the choice of most of the previous shear-flow simulations using the FCT numerical model. The dependence of the results on D_c is then discussed at the end of the section.

Shear flows are highly unstable, and in order to compare the development of the mixing layer with theoretical results, we need to isolate the laminar (viscous) growth of the mixing layer from the growth due to the Kelvin–Helmholtz instability. An unavoidable initial mismatch due to discretization between flow and boundary conditions near the inflow introduces small transverse velocity perturbations which excite the Kelvin–Helmholtz instability in the shear layer near the inflow boundary [3]. This initial instability is subsequently followed by vortex roll-up and global self-sustained instabilities, in which new vortex roll-ups are triggered in the initial shear layer by pressure disturbances originating in the fluid accelerations down-

stream [13]. To ensure that the spread of the streamwise velocity profile is due only to the residual numerical diffusion of the algorithm, we have chosen to *force* the transverse velocity to maintain its initial and inflow value (zero) throughout the computational domain during the simulations.

Since the FCT shear-flow model is nearly inviscid, the model is expected to be meaningful for high-Reynolds-number transitional flow regimes—in which the large-scale flow features are independent of Reynolds number (Re). The approach used to obtain measures of the effective residual numerical viscosity involves approximations which become valid in this limit of high Re, where $v/u = \mathcal{O}(\delta) = \mathcal{O}(1/\mathrm{Re})$, and δ is the thickness of the mixing layer. This approach is also consistent with the thin-shear-layer approximations used to derive Eq. (14) from the incompressible Navier–Stokes equations. In particular, as in boundary layer theory, the viscous diffusion term proportional to $\partial^2u/\partial y^2$ is the dominant one in this limiting flow-regime, and also responsible for the observed numerical spread of the simulated mixing layer in the framework of the present study, where the streamwise gradients are much smaller.

With an explicit unsteady model we can not practically afford to deal with very small Mach numbers because the small timesteps dictated by the Courant condition for numerical stability determine very long corresponding runs to reach steady state. A compromise choice in this work in order to have practical calculations and at the same time nearly incompressible flow is to use mean free Mach numbers, $\mathcal{M} \sim 0.3$–0.4, for which the compressibility effects as measured by the relative mass-density variations $\Delta\rho/\rho \sim \mathcal{M}^2/2$ [14], are at most of the order of 4–8%.

Figure 2 shows the flow configuration for the simulated mixing layer consisting of two coflowing streams of air entering a long chamber, where the separation between walls is chosen sufficiently large to ensure that the mixing layer growth is unaffected by their presence. Inflow and outflow boundary conditions are imposed where appropriate in the streamwise direction (x), and reflecting free-slip wall boundary conditions are required in the transverse direction (y).

The inflow and outflow boundary conditions were developed and tested for multidimensional FCT calculations [1–3]. The inflow boundary conditions specify the density and velocity of the jet and impose an homogeneous Neumann condition on the energy. These conditions are
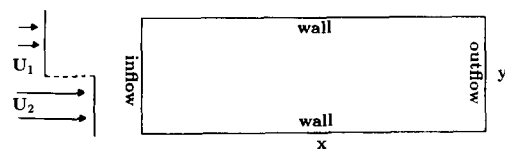

FIG. 2. Flow configuration for the simulated mixing layer.

implemented at the inflow by specifying the guard-cell values for the mass and velocity densities,

$$\rho_{G_1} = \rho_{inflow},\qquad(21a)$$

$$u_{G_1} = u_{inflow} = U(y),\qquad(21b)$$

$$v_{G_1} = 0,\qquad(21c)$$

and imposing a floating condition on the pressure,

$$P_{G_1}^n = P_1^{n-1},\qquad(21d)$$

where the subscripts G_1 and 1 refer to the guard cells and to the first row of cells inside the computational domain (at the inflow), respectively. The guard-cell values of the energy are calculated through the equation of state as a function of the mass density, momenta, and pressure. By imposing a floating condition on the pressure at the inflow, finite (unsteady) cross-stream pressure differences are allowed to appear in the initial shear layer in response to acoustic waves generated by fluid accelerations downstream.

The boundary conditions at the open boundary downstream approximate the time-dependent flow equations at the boundaries, by linearizing the inviscid flow equations and reducing them to advection equations in the outflow direction (x),

$$\partial Q/\partial t + u_{loc}\,\partial Q/\partial x = 0,\qquad(22)$$

where u_{loc} is the local x-component of the velocity near the boundary. This equation is discretized by a first-order upwind scheme. The result is a relation between the outflow guard-cell value $Q_{G_N}^n$ as a function of $Q_{G_N}^{n-1}$ and Q_N^{n-1},

$$Q_{G_N}^n = Q_{G_N}^{n-1}(1-\varepsilon) + \varepsilon Q_N^{n-1},\qquad(23)$$

where n and $n-1$ denote the current and previous integration cycles, and N corresponds to the boundary cell [2]. In addition,

$$\varepsilon = u_{loc}\,\Delta t/\Delta x_N,\qquad(24)$$

where Δt is the integration timestep, and Δx_N is the size of the computational cell at the outflow boundary. The outflow conditions specified by Eq. (23) are imposed on the mass- and momentum-density variables. Information about how the flow relaxes to ambient conditions is provided by specifying the ambient pressure P_{amb} at infinity and imposing a relaxation rate on the pressure [1, 3]. The guard-cell value of the pressure is defined through the expression $P_{G_N} = P_N + (P_{amb} - P_N) \times \Delta x_N/x_{G_N}$. This defines P_{G_N} by interpolating between the pressure value at the Nth cell and the value P_{amb} specified at infinity. The guard-cell

values of the energy are then calculated through the equation of state as a function of the other flow quantities. The inflow conditions allow the pressure at the inflow to vary in response to pressure waves generated by events downstream. An important result of allowing this feedback to occur is that physical, self-sustained global instabilities can occur naturally in the calculations [13].

Since the numerical diffusion depends on the grid spacing, the latter is kept constant in the region of shear layer development. Twenty or more evenly spaced computational cells are used in the transverse direction in the neighborhood of the center of the shear layer, which is initially defined by a (one-cell) step-function discontinuity. Other cases, involving nonsquare uniform griddings and geometrical stretching in the streamwise direction are also considered in order to specifically investigate the effects of non-uniformities. The particular features of the computational grids used in this work are summarized in Fig. 3. The actual dimensions of each domain in Fig. 3 are chosen in such a way to ensure computational efficiency while allowing an adequate description of the evolution of the
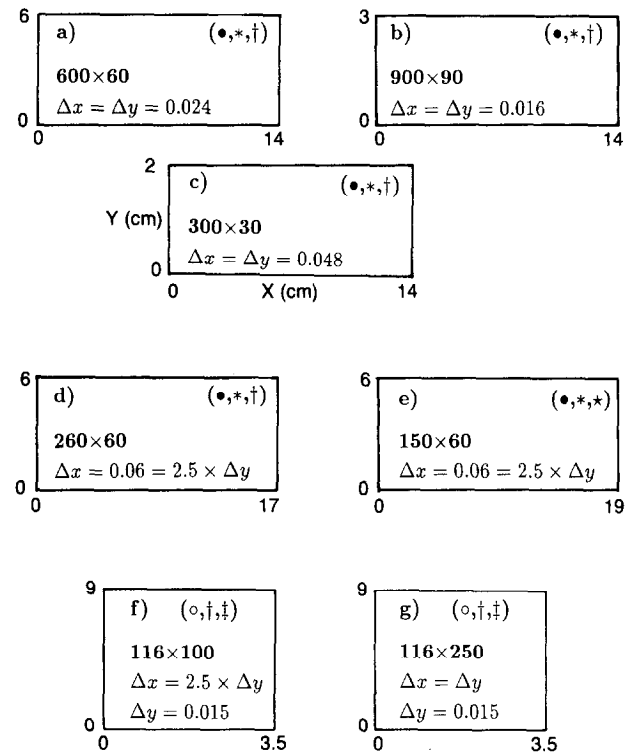

FIG. 3. Computational domains and grids used in the mixing layer simulations: $\bullet$, $c = (U_2 + a)\,\Delta t/\Delta y = 0.46$; $*$, 20 evenly spaced computational cells are used in the y-direction around the shear; wall boundaries are approached through geometrical stretching of the grid (stretching factor = 1.15); $\dagger$, Gridding in x-direction is uniform; $\star$, Grid is geometrically stretched in x-direction for $x > 4$ (stretching factor = 1.03); $\bigcirc$, $c = 0.4$; $\ddagger$, 60 evenly spaced cells are used in the y-direction around the shear; wall boundaries are approached through geometrical stretching of the grid (stretching factor = 1.15).

shear layers. The timesteps used in the calculations are determined from the free-stream conditions by imposing Courant numbers in the range 0.1–0.46.

study the spreading of $u(y)$ from an initial step-function velocity profile at $x = 0$ as a function of streamwise distance x, in terms of the free-stream velocity ratio, gridding, and Courant number. In each case, the time-evolution of the calculations is pursued long enough to ensure that the initial transients flow out of the computational domain and a steady state regime is attained. We reduce the calculated profiles of normalized streamwise momentum $\tilde{g} = (\rho u)/(\rho_0 U_2)$ at different streamwise locations with the similarity variable, $\eta = y(xv/U_2)^{-1/2}$, where $\rho \approx \rho_0 =$ ambient mass density, and v is an adjustable viscosity parameter. The effective numerical diffusion v_e is defined to be equal to the viscosity parameter giving the best fit of $\tilde{g}(\eta)$ to the laminar mixing layer solution $g(\eta) = u/U_2$. The fit is based on the least rms deviations σ_1 and σ_2 defined by

$$\sigma_1^2(v) = \frac{1}{N_x N_y} \sum_{l=1}^{N_y} \sum_{i=1}^{N_x} J \left[\tilde{g}(\eta_{l,i}) - g(\eta_{l,i}) \right]^2, \qquad (25)$$

$$\sigma_2^2(v) = \frac{1}{(N_x - 1)(N_y - 1)}$$

$$\times \sum_{l=1}^{(N_y-1)} \sum_{i=1}^{(N_x-1)} \left[(\Delta \tilde{g}(\eta_{l,i}) - \Delta g(\eta_{l,i}))/\Delta \eta_{l,i} \right]^2, \qquad (26)$$

where $\eta_{l,i} = \eta_{l,i}(v) = y_l(x_i v/U_2)^{-1/2}$, $[y_1, y_2, ..., y_{N_y}]$ and $[x_1, x_2, ..., x_{N_x}]$ are the fixed streamwise and cross-stream

sampling locations, respectively, and Δ is the difference operator, $\Delta H(i) = H(i + 1) - H(i)$. This approach is intended to obtain a quantitative global measure of the effective numerical diffusion of the algorithm and to examine the extent to which the numerically simulated profiles can be reduced to a similarity solution. The procedure is expected to give an estimated effective Reynolds number associated with the (small) scales of the order of a few computational cells.

Typical results corresponding to simulations with $\lambda = 5$ in grid a of Fig. 3 are shown in Fig. 4. Figure 4a shows the behavior of σ_1 and σ_2 as a function of v. Associated with the particular grid chosen, the figure shows least deviations for $v = v_e \approx 0.16 \text{ cm}^2\text{sec}^{-1}$, corresponding to air viscosity at the standard temperature and pressure conditions of the simulations. Profiles of $\tilde{g}(\eta)$ are compared with $g(\eta)$ in Fig. 4b, where the markers correspond to actual grid points and distinguish between different streamwise stations. The spreading of the initial step-function profile is essentially confined within 3–5 computational cells for the range of streamwise locations considered, and the calculated points collapse quite well in the vicinity of the theoretical curve. The optimal fit in this case leads to an effective Reynolds number, $\text{Re}_{\text{eff}} = \bar{U}\delta/v_e \approx 1800$, where $\bar{U} = (U_1 + U_2)/2$, and $\delta = \delta y$, is taken to be the initial thickness of the shear layer. Based on Eq. (12), with $U_2 = 2.0 \times 10^4$ cm/sec, $a = 3.5 \times 10^4$ cm/sec, and $c = 0.5$, the local estimate of the numerical diffusion $\mathscr{D}$ for this case turns out to be nearly three times larger than v_e. A larger local prediction for the effective numerical diffusion is expected, since Eq. 12) will estimate the transverse numerical diffusion of the shear
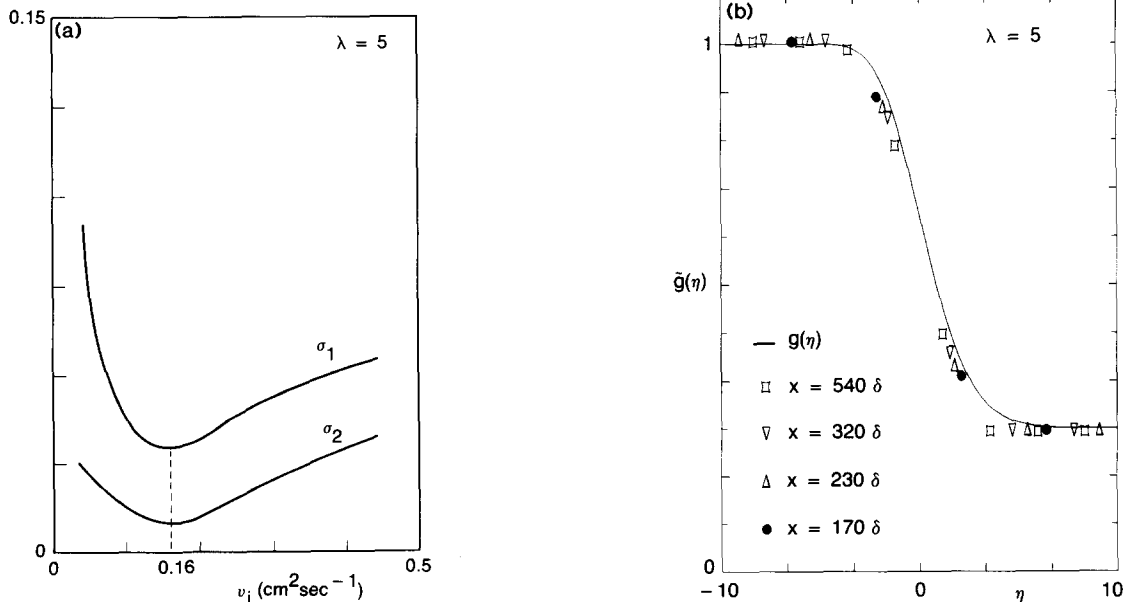

FIG. 4. Mixing layer simulation on grid a in case $\lambda = 5$, $D_c = 0.999$. (a) Root-mean-square deviations σ_1 and σ_2. (b) Comparison of momentum profiles $\tilde{g}(\eta)$ for $v_e = 0.16 \text{ cm}^2\text{sec}^{-1}$ at selected streamwise locations with profile ($g(\eta)$) predicted by boundary layer theory.

without accounting for the streamwise convection of the fluid elements.

The numerical diffusion is slightly different on each side of the shear layer. This can be observed in Fig. 4b for $\lambda = 5$, which suggests that the diffusivity is smaller on the slower side ($\eta > 0$). The dependence of this diffusivity difference as a function of free-stream velocity ratio λ can be obtained by examining the partial rms deviations σ_{1+} and σ_{1-}, corresponding to $\eta > 0$ and $\eta < 0$, respectively, defined by

$$\sigma_{1\pm}^2(v) = \frac{1}{N_x N_y} \sum_{\pm \eta_{l,i} \geqslant 0} [\tilde{g}(\eta_{l,i}) - g(\eta_{l,i})]^2. \qquad (27)$$

In Fig. 5 we plot σ_1, σ_{1+}, σ_{1-} for the extreme values of velocity ratio considered here, namely for $\lambda = 2$ and $\lambda = \infty$. The separation between the minima of σ_{1+} and σ_{1-} can be used to measure the difference between the numerical diffusivities on each side of the shear layer. These differences are less pronounced for the case $\lambda = 2$ with more nearly similar free-stream velocities, and can be attributed to a small streamwise-velocity-dependent contribution to the global numerical diffusion, associated with the integration in the x-direction. The origin of this contribution can be understood locally by noting that the antidiffusion will never cancel the diffusion exactly at the end of the FCT cycle if convection cannot be neglected (cf. Eqs. (4) and (8)). A local analysis similar to that in Section 3.1 shows the presence of an additional velocity-dependent diffusion term with expected behavior of the form $\mathcal{O}(c\delta x u^2)$, which is con-

sistent with the observed (global) differences. Alternatively, velocity-dependent discrepancies between numerical and theoretical results can also be expected to some extent due to the fact that the flow is solenoidal in the theoretical (incompressible) case, whereas the regime of the computations is characterized by low, but finite, Mach number. More specifically, in the framework of the present computations, $\partial v/\partial y$ is independent of $\partial u/\partial x$ and vanishes by construction, so that the computed velocity field has a non-zero divergence, $\nabla \cdot \mathbf{u} = \partial u/\partial x \neq 0$. Thus, zones of positive (negative) divergence appear during the development of the mixing layer, as the top (bottom) stream accelerates (decelerates), which could also explain the larger (smaller) diffusivity observed in the computed profiles.

Figure 6 shows the dependence of the rms deviations σ_1 on the free-stream velocity ratio λ in grid a of Fig. 3 for fixed $U_2 = 2 \times 10^4$ cm sec^{-1}. The optimal value v_e is not very sensitive to changes in λ, which is consistent with the local estimate for the numerical diffusion (Eq. (12)), since $(|\mathbf{v}| + a)_{\text{peak}}$ is the same for all cases.

Figure 7 shows the typical linear dependence of v_e on the diffusion parameter D_c, in qualitative agreement with the linear dependence on $(1 - D_c)$ predicted by the local estimate (Eq. (12)), but with a slope significantly smaller (e.g., of the order five times smaller on grid a, for $\lambda = 5$). As pointed out above, a smaller actual effective diffusivity than that predicted by Eq. (12) can be attributed to the fact that the latter accounts for the local cross-stream transverse numerical diffusion of the mixing layer when no streamwise convection is present.
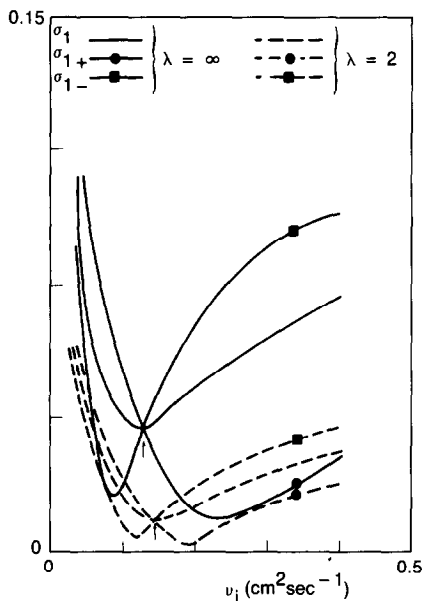

FIG. 5. Mixing layer simulation on grid a. Dependence of diffusivities on each side of the shear layer on velocity ratio λ for $D_c = 0.999$. The arrows indicate least values of σ_1 at intersections of curves of partial deviations σ_{1+} and σ_{1-}.
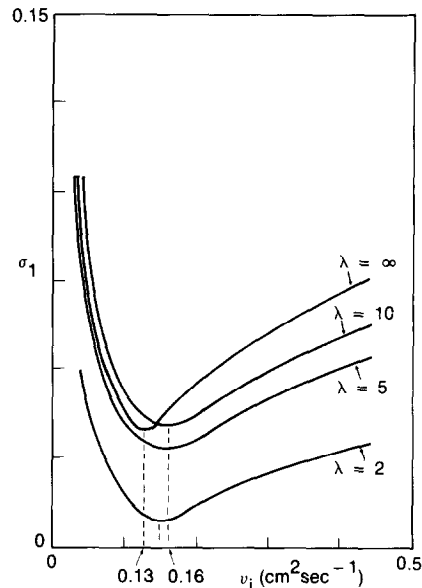

FIG. 6. Mixing layer simulation on grid a for $D_c = 0.999$. Dependence of global numerical diffusion on velocity ratio λ.
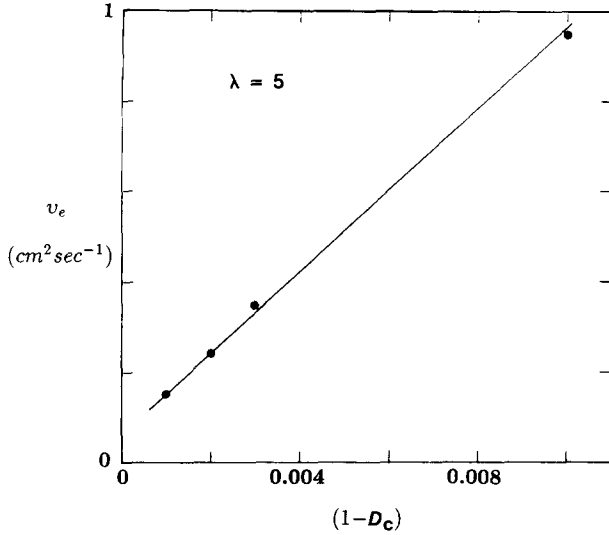
FIG. 7. Mixing layer simulation on grid a. Dependence of global numerical diffusion on diffusion parameter D_c.

Figure 8 shows a comparison similar to that in Fig. 4b ($D_c = 0.999$), for the case $D_c = 0.990$, corresponding to the highest value of v_e in Fig. 7. The spreading of the step-function is now significantly faster, i.e., involves more computational cells at shorter distances from the origin than those considered in Fig. 4b. The results also indicate that an improved agreement with the theoretical slope is attained as the effective numerical diffusion v_e increases.
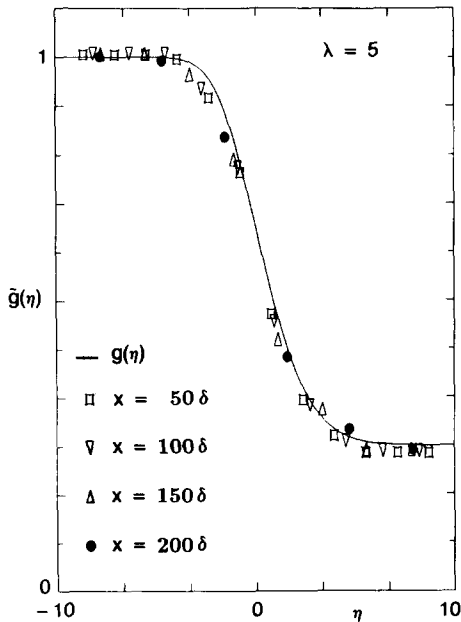
FIG. 8. Mixing layer simulation on grid a in case $\lambda = 5$, $D_c = 0.990$. Comparison of momentum profiles $\bar{g}(\eta)$ for $v_e = 0.16 \text{ cm}^2\text{sec}^{-1}$ at selected streamwise locations with profile $(g(\eta))$ predicted by boundary layer theory.
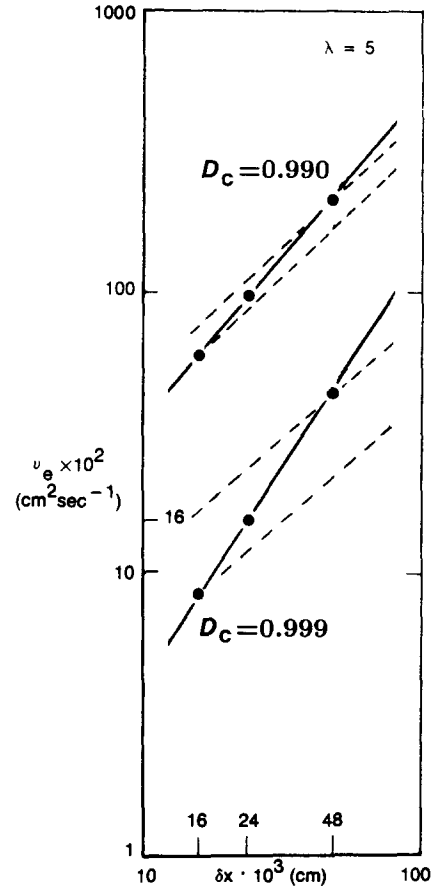

FIG. 9. Mixing layer simulation on grids a–c, $\lambda = 5$. Dependence of global numerical diffusion on grid spacing for $D_c = 0.990$, 0.999. The dashed lines have the slope $\alpha_1 = 1$ predicted by Eq. (12).

Figure 9 shows the effect of grid spacing on the rms deviations for $\lambda = 5$, by considering a finer (Fig. 3b) and a coarser grid (Fig. 3c) than that used for the cases in Fig. 5 (grid a in Fig. 3), with spacings twice as large and one-and-a-half times smaller, respectively. The observed growth of v_e in Fig. 7 implies a *nonlinear* dependence on grid spacing δx,

$$v_e \sim (\delta x)^{\alpha_1}, \tag{28}$$

where $\alpha_1 = \alpha_1(D_c)$ decreases from $\alpha_1 = 1.48$ to $\alpha_1 = 1.16$ when D_c is reduced from 0.999 to 0.990, approaching the value $\alpha_1 = 1$ (predicted by Eq. (12)) as v_e increases. Thus, in calculations performed with fixed c, and when the initial velocity profile is defined by a smooth function in such a way that the initial shear layer thickness is grid-independent, Eq. (28) implies an increase in effective Reynolds number with grid refinement ($\delta x \to 0$) according to

$$\text{Re}_{\text{eff}} \sim \delta x^{-\alpha_1(D_c)}. \tag{29a}$$

In the case of the initial step-function velocity profile considered in this work, for which the initial thickness of the shear layer is of order δx, we get

$$\mathrm{Re}_{\mathrm{eff}} \sim \delta x^{1 - \alpha_1(D_c)}, \qquad (29b)$$

whereas Eq. (12) implies a value independent of grid size for $\mathrm{Re}_{\mathrm{eff}}$. The dependence of the effective numerical diffusion on the Courant number is shown in Fig. 10 for grid c in Fig. 3. The results now suggest the nonlinear dependence

$$v_e \sim c^{-\alpha_2(D_c)}, \qquad (30)$$

where $\alpha_2 = \alpha_2(D_c)$ increase from $\alpha_2 = 0.49$ to $\alpha_2 = 0.83$ when D_c decreases from 0.999 to 0.990, in contrast with the inversely proportional dependence on Courant number in Eq. (12). As noted above, the functional behavior predicted by Eq. (12) ($\alpha_2 = 1$) is approached for larger values of v.

The effects of non-uniformities on the gridding are examined in Figs. 11–13 for $D_c = 0.999$. We first examine the effects of changing the aspect ratio $\delta x/\delta y$ of the grid while maintaining it evenly spaced in each direction. The plot of rms deviations in Fig. 11 suggests that changing from $\delta x/\delta y = 1$ (grid a of Fig. 3) to $\delta x/\delta y = 2.5$ (grid d of Fig. 3) does not significantly affect the nature of the effective numerical diffusion. This is physically expected to some extent. It indicates that for aspect ratios $\delta x/\delta y \gtrsim 1$, v_e is essentially determined by the (numerical) viscous term proportional to $\partial^2 u/\partial y^2$ introduced by the algorithm. In Fig. 12 we include results obtained on grids d and e of
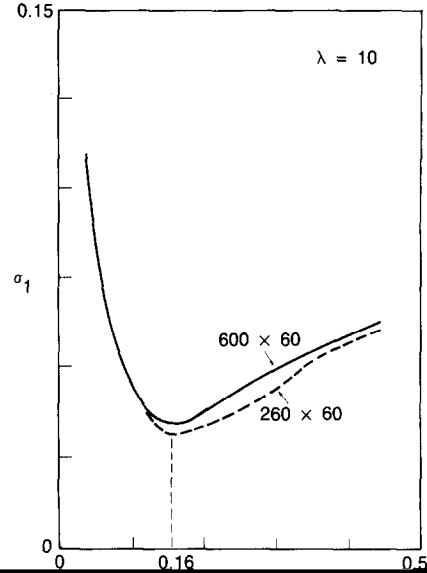

FIG. 11. Mixing layer simulation on grids a and d, $\lambda = 10$, $D_c = 0.999$. Dependence of global numerical diffusion on gridding aspect ratio.

Fig. 3, both having a basic gridding aspect ratio 2.5 which is maintained throughout the region of interest in one case and geometrically increased in a significant portion of the domain in the other. As can be expected, the results indicate that if much larger non-uniformities in the gridding are introduced through grid stretching, the numerical term associated with $\partial^2 u/\partial x^2$ can no longer be considered negligible and the effective diffusion can consequently become significantly larger than in the uniform case.
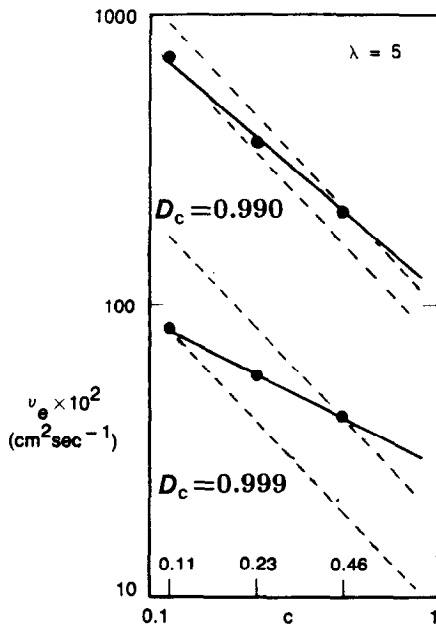

FIG. 10. Mixing layer simulation on grid c, $\lambda = 5$. Dependence of global numerical diffusion on Courant number for $D_c = 0.990, 0.999$. The dashed lines have the slope $\alpha_2 = 1$ predicted by Eq. (12).
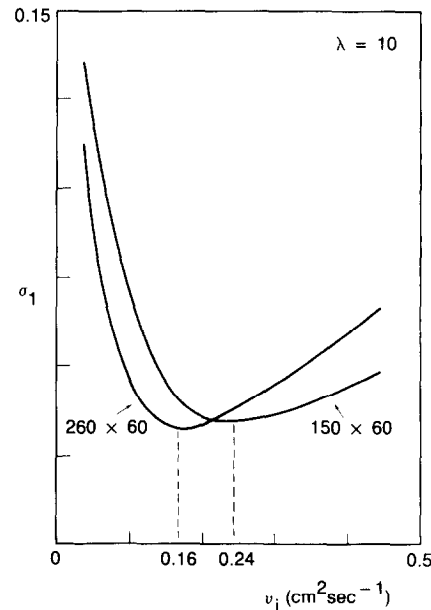

FIG. 12. Mixing layer simulation on grids d and e, $\lambda = 10$, $D_c = 0.999$. Effects of grid stretching in x-direction on global numerical diffusion.
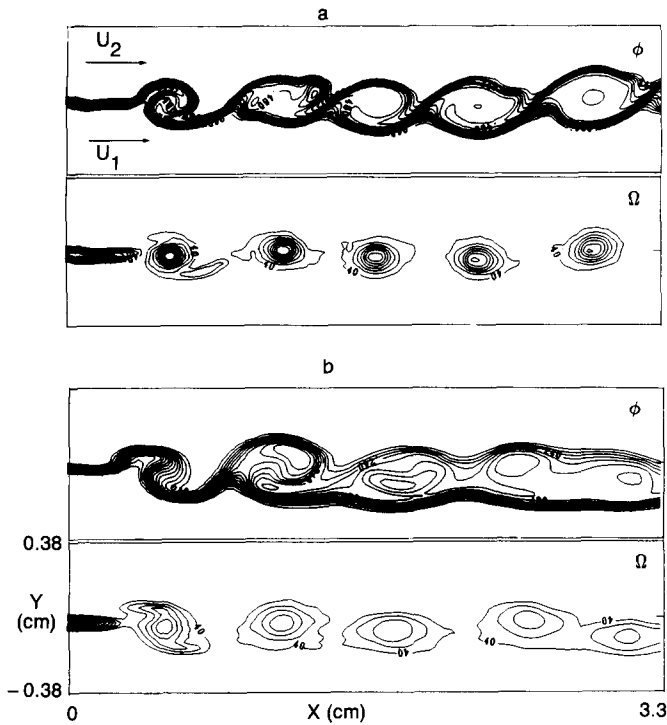
FIG. 13. Fully two-dimensional mixing layer simulation for $\lambda = 5$. Effects of gridding aspect ratio on global numerical diffusion for $D_c = 0.999$. (a) $\delta x = \delta y$ (grid f); (b) $\delta x = 2.5\delta y$ (grid g). Instantaneous flow visualization in terms of contours of vorticity (upper frame) and of a passive scalar convected with the flow velocity (lower frame). The contour intervals for each flow quantity are the same in (a) and (b).

In order to further assess the dependence of the effective numerical viscosity on the gridding aspect ratio, we examine the results of planar shear-flow simulations also initialized with a step-function velocity profile, but for which the zero-transverse-velocity restriction is not enforced, so that vortex roll-up can now take place. Figure 13 shows typical instantaneous visualizations using contours of vorticity (Ω) and of a passive scalar (ϕ) convected with the flow velocity, where ϕ is defined to be initially zero for the slower stream and unity for the faster stream. The calculations are performed on grids f and g of Fig. 3, and the flow is organized by adding a small time-dependent perturbation to the stream-wise velocity at the inflow with frequency equal to that of the most unstable mode. The figure shows the presence of vortex rolls resulting from the evolution of the nonlinear Kelvin–Helmholtz instability. The frames shown are associated with the same physical time, and identical conditions except for the uniform gridding, which involves aspect ratio $\delta x/\delta y = 1$ in one case (Fig. 13a), and $\delta x/\delta y = 2.5$ in the other (Fig. 13b). In both simulations, the Courant number is $c = 0.4$, $\delta y = 0.015$ cm, and $\lambda = 5$, with air streams under the same temperature and pressure conditions as in the cases discussed previously. In particular, the conditions of the simulations are such that the expected numerical

diffusivities in the case with $\delta x/\delta y = 1$ are nearly the same as those found in the more resolved case of Fig. 9 (for $D_c = 0.999$, and $\delta x = \delta y = 0.016$ cm). For each flow quantity, the contour intervals are chosen to be the same in Figs. 13a and 13b. The effects of numerical diffusion on the flow can then be inferred by examining the spreading of the high-strain region at the interface between the two streams of ϕ based on the distribution and density of contours, and by examining the numerical stability of the vortical structures based on the vorticity contours. In turn, v_e—based on the comparison of the laminar computed and theoretical solutions—gives us an indication of the amount of diffusion responsible for that spreading.

In the case of the calculation on grid f (aspect ratio unity), numerical diffusion effects are responsible for the initial spreading of the step-velocity profile onto an inflectional profile confined within 3–5 computational cells and are otherwise essentially negligible further on downstream, as shown in Fig. 13a. In this case, the numerical diffusion effects are isotropic, they preserve the large-scale features of the flow without significant distortion, and thus mimic very small physical-viscosity effects. Although the general features of the flow are similar in both calculations, it is apparent that Fig. 13b, for which $\delta x/\delta y = 2.5$, shows considerably larger numerical diffusion effects. This is indicated by the significant spreading of the high-strain regions (particularly on the faster side) and by the increasingly poor resolution of the vortex rolls in terms of vorticity contours as we move downstream. This is in contrast with the results in Fig. 11, suggesting that no significant differences should be expected between calculations on grids f and g. A major difference, however, is that the strain direction is now not necessarily restricted to the transverse direction, and when $\delta x > \delta y$ the high-strain region is diffused more in the x-direction than in the y-direction.

4. CONCLUSIONS

We have shown that the nonlinear residual numerical diffusion of the FCT shear-flow model with $D_c \lesssim 1$ can emulate the effects of physical viscosity. Effective (global) measures of the numerical viscous diffusion in the model, v_e, were obtained by comparing the numerical spread of low-Mach-number simulated mixing layers with the theoretical spread predicted by boundary layer theory. Associated with v_e, the profiles of calculated x-momentum at different streamwise locations collapse quite well in the vicinity of the theoretical results when plotted as a function of the similarity variable η. We found that the global numerical diffusion is not very sensitive to changes in free-steam velocity ratio λ, and can be reduced to a desired level by refining the grid spacing. For example, for $D_c = 0.999$, when using the uniform grid a in Fig. 3, and depending on λ, the optimal v_e was found to

vary within a range of 80%–100% of the physical viscosity value for air at the temperature and pressure conditions of the simulations.

When nonsquare uniform grids are used, the numerical diffusion is not isotropic and the present approach for its global interpretation is difficult to implement, although it can conceivably be used to obtain bounds on its magnitude. We found that the large-scale features of the shear flow can be significantly distorted by the effects of the non-isotropic numerical diffusion. These results suggest that in inviscid simulations of shear flows where numerical diffusion is the only cause of momentum diffusion, grids with aspect ratios as close to unity as possible should be used to minimize spurious flow distortions. This requirement can be clearly relaxed when viscous terms are included in the model and the grid size is chosen to ensure that numerical diffusion is negligible as compared to physical diffusive effects.

ACKNOWLEDGMENTS

REFERENCES

1. J. P. Boris, E. S. Oran, J. H. Gardner, F. F. Grinstein, and C. E. Oswald, in *Ninth International Conference on Numerical Methods in Fluid Dynamics*, edited by Soubbaramayer and J. P. Boujot, (Springer-Verlag, New York, 1985), p. 98.

2. F. F. Grinstein, R. H. Guirguis, J. P. Dahlburg and E. S. Oran, in *11th International Conference on Numerical Methods in Fluid Dynamics*, edited by D. L. Dwoyer, M. Y. Hussaini, and R. G. Voigt (Springer-Verlag, New York, 1989), p. 283.

3. F. F. Grinstein, E. S. Oran, and J. P. Boris, *J. Fluid Mech.* **165**, 201 (1986).

4. F. F. Grinstein, E. S. Oran, and J. P. Boris, *AIAA J.* **25**, 92 (1987).

5. F. F. Grinstein, F. Hussain, and E. S. Oran, *Eur. J. Mech. B/Fluids* **9**, 499 (1990).

6. F. F. Grinstein, F. Hussain and E. S. Oran, AIAA Paper 89-0977, Washington DC, 1989 (unpublished).

7. F. F. Grinstein, E. S. Oran, and A. K. M. F. Hussain, in *Proceedings of the 6th Symposium on Turbulent Shear Flows, Toulouse, France, September 6–9, 1987*; see also AIAA Paper 88-0042, Washington, DC, 1988 (unpublished).

8. J. P. Boris, and D. L. Book, in *Methods in Computational Physics, 16*, edited by J. Killeen (Academic Press, New York, 1976), p. 85.

9. D. L. Book, J. P. Boris, and S. T. Zalesak, in *Finite-Difference Techniques for Vectorized Fluid Dynamics Calculations*, edited by D. L. Book (Springer-Verlag, New York, 1981), p. 29.

10. J. P. Boris, Laboratory for Computational Physics & Fluid Dynamics, Naval Research Laboratory, Washington, DC, private communication (1988).

11. S. T. Zalesak, in *Advances in Computer Methods for Partial Differential Equations, IV*, edited by R. Vichnevetsky and R. S. Stepleman (IMACS, Rutgers University, New Brunswick, 1981), p. 126.

12. H. Schlichting, *Boundary Layer Theory* (McGraw-Hill, New York, 1987), p. 183.

13. F. F. Grinstein, E. S. Oran, and J. P. Boris, *Phys. Rev. Lett.* **64**, 87 (1990).

14. H. Schlichting, *Boundary Layer Theory* (McGraw-Hill, New York, 1987), p. 10.